ARTICLE

Near-Infrared Polarimetric Image Sensors Based on Ordered Sulfur-Passivation GaSb Nanowire Arrays

Kai Zhang,[‡] Zhihui Ren,[‡] Huichen Cao, Lingling Li, Ying Wang, Wei Zhang, Yubao Li,* Haitao Yang, You Meng, Johnny C. Ho,* Zhongming Wei,* and Guozhen Shen*

Read Online

ACCESS | Metrics & More | Article Recommendations | Supporting Information

ABSTRACT: The near-infrared polarimetric image sensor has a wide range of applications in the military and civilian fields, thus developing into a research hotspot in recent years. Because of their distinguishing 1D structure features, the ordered GaSb nanowire (NW) arrays possess potential applications for near-infrared polarization photodetection. In this work, single-crystalline GaSb NWs are synthesized through a sulfur-catalyzed chemical vapor deposition process. A sulfur-passivation thin layer is formed on the NW surface, which prevents the GaSb NW core from being oxidized. The photodetector based on sulfur-passivation GaSb (S-GaSb) NWs has a lower dark current and higher responsivity than that built with pure GaSb NWs. The photodetector exhibits a large responsivity of 9.39×10^2 A/W and an ultrahigh detectivity of 1.10×10^{11} Jones for 1.55 μm incident light. Furthermore, the dichroic ratio of the device is measured to reach 2.65 for polarized 1.55 μm light. Through a COMSOL simulation, it is elucidated that the origin of the polarized photoresponse is the attenuation of a light electric field inside the NW when the angle of incident polarization light rotates. Moreover, a flexible polarimetric image sensor with 5 × 5 pixels is successfully constructed on the ordered S-GaSb NW arrays, and it exhibits a good imaging ability for incident near-infrared polarization light. These good photoresponse properties and polarized imaging abilities can empower ordered S-GaSb NW arrays with technological potentials in next-generation large-scale near-infrared polarimetric imaging sensors.

**KEYWORDS:** GaSb, nanowire arrays, sulfur-passivation, polarized photodetector, imaging sensor
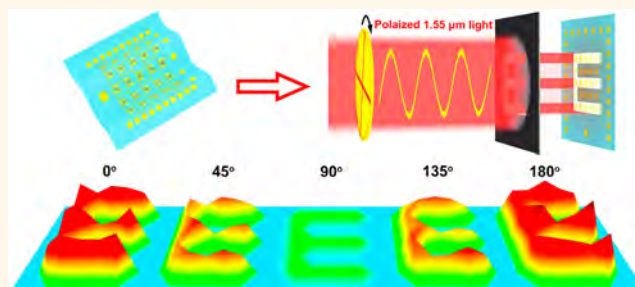
With innovations in detection and sensing science, multidimensional optical detection technology has come into being. The polarimetric imaging sensor can extend the detection of photoelectric signal from light wavelength and intensity to a light polarization vector, which exhibits application potentials in remote sensing image, environmental monitoring, agriculture, and medical detection.[1−3] Recently, near-infrared polarization photodetectors (780−2526 nm) based on low-symmetry 2D/1D materials have become a research hotspot because the near-infrared light is not affected by smoke or clouds in the atmosphere.[4−8] To date, some narrow-bandgap 2D/1D materials have been explored as near-infrared polarization photodetectors successfully because of the anisotropic photoresponse ascribed to the low-symmetry crystal structure, such as black phosphorus (b-P),[9] As−P,[10] PdPS,[4] NbS3,[5] GeSe,[11] GaAs,[8] Te,[6] Sb2S3,[7] ZnTe,[12] etc. In particular, III−V semiconductor nanowires (NWs) that are appropriate for contemporary silicon technology also have polarized photoresponse properties

resulting from their anisotropic 1D geometry structure.[13,14] They display an anisotropic photoresponse for linear polarization light as long as the energy of the incident light is larger than that of the NW bandgap.[12,13,15] However, there are few reports about near-infrared polarization photodetectors based on narrow-bandgap III−V NWs. Furthermore, because of their distinguishing 1D structure features, narrow-bandgap III−V NWs can be assembled to ordered NWs arrays which could be constructed as flexible near-infrared polarimetric image sensors.[14,16,17] They possess the advantages of light weight, portability, and low cost compared with the commercial
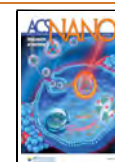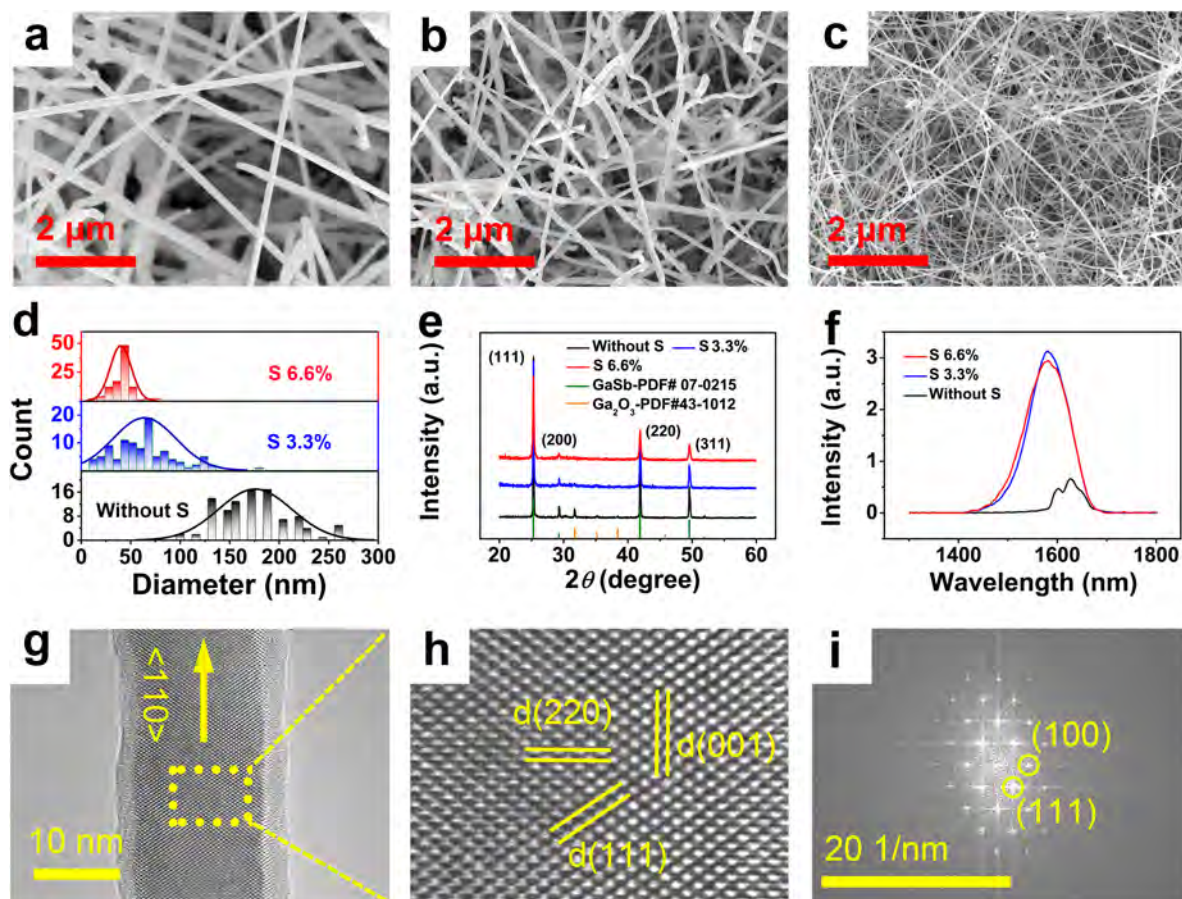
Figure 1. Characterization of as-grown S-GaSb NWs. SEM images of (a) pure GaSb NWs, (b) S-GaSb NWs with S 3.3 mass percent in the precursor, (c) S-GaSb NWs with S 6.6 mass percent in the precursor. (d–f) Diameters distribution, XRD, PL spectra (77K) of pure GaSb NWs, S-GaSb NWs with S 3.3 mass percent in the precursor, S-GaSb NWs with 6.6 mass percent in the precursor. (g) TEM image of a S-GaSb NWs with S 6.6 mass percent in the precursor. (h,i) HRTEM and FFT images of the rectangular area in (g).

polarization detection systems consisting of lens and circuit systems.[17−19] More in-depth research is needed and expected.

GaSb NWs are technologically important narrow-bandgap III−V semiconductors ascribed to the physical properties of direct bandgap (∼0.726 eV), zinc blende structure, p-type conductivity, and high hole mobility. They have been explored to build high-performance field-effect transistors (FETs) and near-infrared photodetectors.[20−23] Because of the intrinsic light polarization sensitivity, GaSb NWs are also good candidates for near-infrared polarization photodetectors.[13,14] Nonetheless, it is still challenging to realize the application of GaSb NW-based photodetectors because of their excessive dark current and the deteriorated surface oxidation, which are also common problems of other III−V semiconductor devices.[24−28] The excessive dark current will result in large device noise, and the deteriorated surface oxidation will trap photogenerated carriers, thus downgrading the photoelectric performance of GaSb NWs-based photodetctors.[24,26] Recently, the reported sulfur-catalyzed growth of GaSb NWs was found to be an effective way to resolve these problems. Compared with pure GaSb NWs, the obtained sulfur-passivation GaSb NWs have thinner diameters, and the S is not doped into the NW core but distributed on the surface.[22,25,29] For instance, in the report of Wang et al., the S-catalyzed chemical vapor deposition (CVD) method was used to grow $GaAs_xSb_{1−x}$ NWs with Sb_xS_y and Ga_xS_y layers being formed on the NWs surface. Impressively, the detectivity (D*) of the photodetector based

on $GaAs_xSb_{1−x}$ NW reached 2.5×10^{10} Jones under 1.55 μm illumination.[21] Unfortunately, the influence mechanism of the surface sulfur-passivation layer for the photoresponse properties of the GaSb NW-based photodetector is still far from clear. In our previous work, the polarized photodetector based on GaSb NW has been explored, where the device exhibited good anisotropy photoresponse for linear polarization of 1.55 μm light. It implies that GaSb NWs arrays have the potential to integrate flexible near-infrared polarimetric image sensors.[23]

In this work, the sulfur-passivation GaSb (S-GaSb) NWs are synthesized through the S-catalyzed CVD process with the mass percentage of S in the precursor being kept at 0%, 3.3%, 6.6%, and 50%, respectively. Under the circumstance that S is 6.6%, the best performances S-GaSb NWs are obtained, and a thin surface S-passivation layer, which would prevent the oxidation of Sb in the NW core, is formed on the NW surface. Compared with pure GaSb NW, the photodetector based on the S-GaSb NW has a lower dark current and higher responsivity. Under the incident near-infrared light of 1.55 and 1.31 μm, the photodetector exhibits the responsivity and detectivity of 9.39×10^2 A/W, 1.10×10^{11} Jones and 1.38×10^3 A/W, 1.61×10^{11} Jones, respectively. The dichroic ratios are measured as 2.65 and 1.85 for the polarized 1.55 and 1.31 μm light. To elucidate the origin of the polarized photoresponse, the COMSOL simulation is conducted. The light electric field will be attenuated when the angle of incident polarization light rotates from being parallel to being
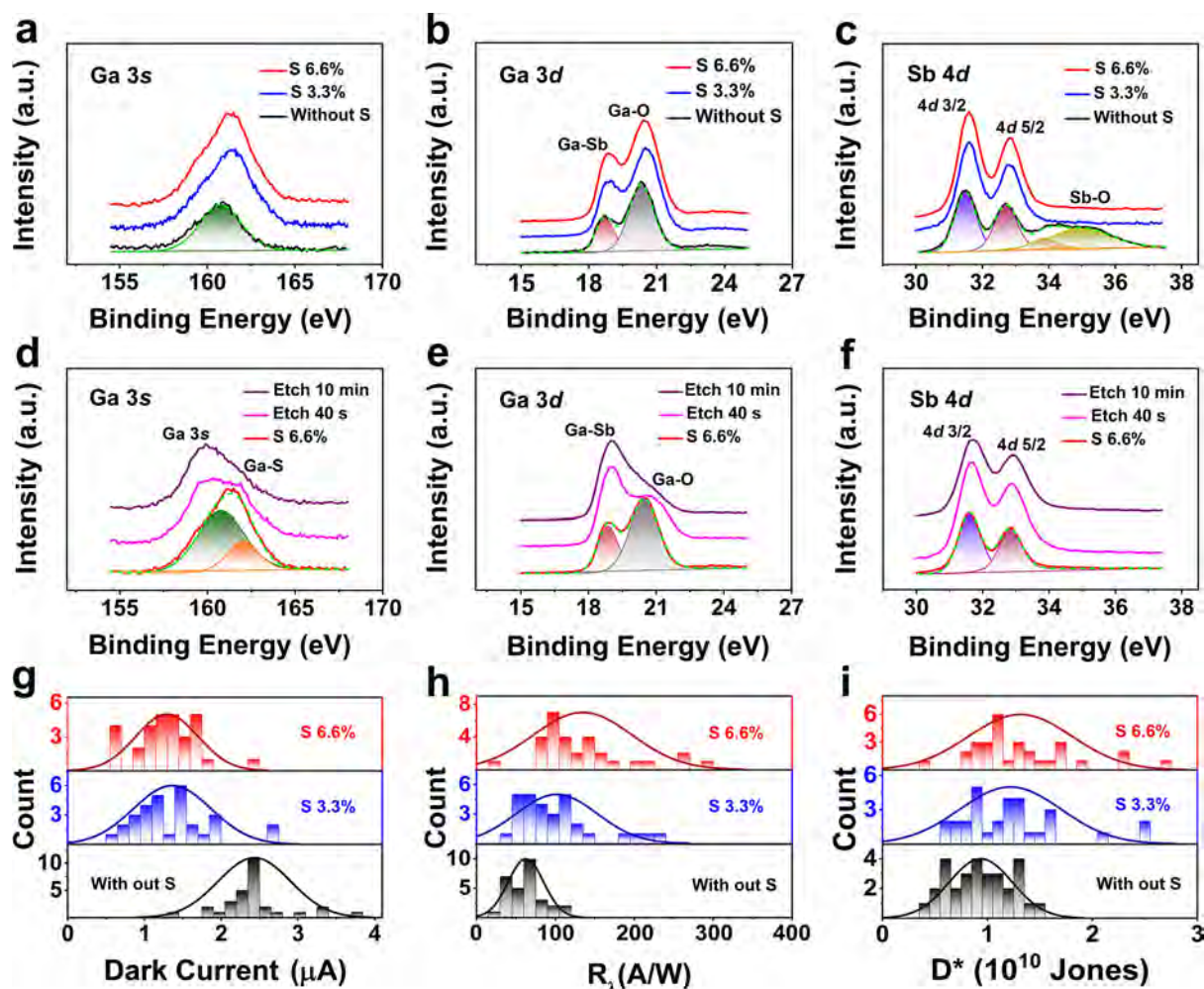
Figure 2. Surface elemental analysis of as-grown S-GaSb NWs and effect of surface S-passivation layer on NWs properties. XPS spectra of as-grown S-GaSb NWs for (a) Ga 3s, (b) Ga 3d, and (c) Sb 4d bonding regions. XPS spectra of S-GaSb NWs with S 6.6% before and after etching for (d–f) Ga 3s, Ga 3d, Sb 4d bonding regions, respectively. Effect of surface S-passivation layer on NW device's (g) dark currents, (h) R_λ, and (i) D*.

perpendicular to the S-GaSb NW long-axis, which is well consistent with our experiment data.[13,15] What's more, ordered S-GaSb NWs arrays are prepared by a contact printing method. A flexible polarimetric image sensor with 5 × 5 pixels is then constructed on the ordered NWs arrays, and the sensor exhibits good polarization imaging ability for incident polarization 1.55 μm light. These polarization photoresponse properties and imaging abilities indicate that the ordered S-GaSb NWs arrays have application potentials in flexible and large-scale near-infrared polarimetric imaging sensors.

RESULTS AND DISCUSSION

To date, the S-catalyzed CVD method to grow GaSb NWs has developed successfully. Using S as the catalyst, GaSb NWs would be grown thinner and longer. In particular, the distribution of the S element is only on the NW surface.[21,22,25,30] In this work, the S element is employed as the surface passivator as well as the growth catalyst in the CVD process. To discover the best experimental conditions, different mass ratios of S power are adopted. In the precursor, the amount of GaSb powers is fixed at 0.3 g, and the S powers are 0, 0.01, 0.02, and 0.3 g, respectively, which represents the mass percentage of S at 0%, 3.3%, 6.6%, and 50%. Here, the S 0%

and 50% are used as control. The process of sulfur-passivation GaSb (S-GaSb) NW growth, as illustrated in Figure S1, will be introduced in the Experimental Section in detail. Parts a–c of Figure 1 are SEM images of the as-grown S-GaSb NWs, corresponding to S 0% (pure GaSb), 3.3%, and 6.6% in the precursor. SEM images taken from the larger area are also shown in Figure S2a–c. It can be seen that NWs have grown in high density for all samples on the Si substrate. The energy-dispersive spectroscopy (EDS) images, corresponding to Figure S2a–c, are displayed in Figure S2d–f. It is obvious that the main peaks of Ga and Sb are detected in all components, and little peaks of S are discovered in the S 3.3% and S 6.6%. Noteworthy, from SEM images, the diameter becomes thinner with an increase in S content. Through a statistical analysis of 100 NWs, the normal distribution of diameters is drawn in Figure 1d. The normal distribution of diameters is 175.7 ± 37.0 nm for pure GaSb NWs, 63.9 ± 31.7 nm for S-GaSb NWs with S 3.3%, and 39.9 ± 10.6 nm for S-GaSb NWs with S 6.6%, respectively. The majority of S-GaSb NWs with S 6.6% are thinner than 50 nm, which indicates the uniform diameter and smooth surface of NWs.[22,25] The crystal phase of as-grown S-GaSb NWs is verified by the X-ray diffraction (XRD) in Figure 1e. All as-grown NWs are in zinc-

blende crystal structures with $a = b = c = 0.6095$ nm (PDF no. 07-0215). However, weak peaks of Ga_2O_3 (PDF no. 43-1012) are also detected in the pure GaSb NWs.[25] With the addition of S in the precursor, these Ga_2O_3 peaks disappear, indicating that high-purity and zinc-blende S-GaSb NWs are finally formed. To further study the effect of the S surface passivation on the NW crystallinity and optical properties, the PL measurement is tested. As shown in the PL spectra (77 K) in Figure 1f, near-infrared emission peaks are observed. In the PL spectrum of pure GaSb NWs, the frequency doubling signal of 1600 nm of excitation light becomes relative apparent due to the PL emission peak. The emission peak become stronger with the increasement of the S in the precursor, which implies the improvement of the crystallinity. As depicted in Figure S3, the peak is 1627 nm (0.762 eV) for pure GaSb NWs, 1581 nm (0.784 eV) for S-GaSb NWs with S 3.3%, and 1581 nm (0.784 eV) for S-GaSb NWs with S 6.6%, respectively. The emission peaks show an obvious blue shift, which is attributed to the quantum confinement effect enhanced with the thinner NW diameter resulting from the S surface passivation.[25,31−35] On the basis of the above-described SEM/EDS/XRD/PL results, with the adoption of an appropriate amount of S in the precursor, the S-GaSb NWs can be grown with thinner diameter, more antioxidation, and higher crystallinity. In this work, we have found that the best condition is with S 6.6 mass % in the precursor.

To further study the microstructure of S-GaSb NWs with S 6.6%, TEM characterization is conducted. Figure 1g is the TEM image of a typical single NW with 20.5 nm diameter, showing that the NW body is covered by an ~3 nm amorphous layer. Parts h and i of Figure 1 are the HRTEM and fast Fourier transform (FFT) taken from the rectangular area of Figure 1g. Without noticeable crystal defects, high-resolution lattice fringes are presented and the spacing distances are measured to 0.21, 0.35, and 0.31 nm corresponding to (220), (111), and (001) lattice planes of the GaSb zinc blende phase (PDF no. 07-0215), which is in good agreement with the aforementioned XRD result. The single zinc blende structure of as-grown S-GaSb NWs with S 6.6% is also confirmed. Moreover, the radial direction is aligned along the (220) plane, which manifests that the axial growth orientation is ⟨110⟩. These results are consistent with the Si NWs and GaSb NWs reported previously, where the ⟨110⟩ growth orientation is favored for the thin NWs and the ⟨111⟩ growth orientation is favored for the thick NWs.[29,36] The STEM and EDS element mapping images of the above S-GaSb NW body are presented in Figure S4. The Ga and Sb element almost have stoichiometry of ~1:1, and both of them are uniformly distributed along the NW body. As the surface passivator as well as growth catalyst, S also can be found on the NW body.

To shed light on the exact distribution of S on the body of as-grown S-GaSb NWs, the X-ray photoelectron spectroscopy (XPS) spectra are performed. Compared to previous reports, a small shift that might be ascribed to size effects is not emphasized herein.[25,37,38] As shown in Figure S5a, all of the XPS peaks are calibrated with the C1s peak (284.8 eV). In Figure S5b, S 2s peaks (226.1 eV) can be found in both S-GaSb NWs with S 3.3% and 6.6% samples. The XPS analysis is focused on typical Ga 3s, Ga 3d, and Sb 4d spectra, which are commonly studied in the literature.[21,25,27,39] In Figure 2a−c, the black curve is pure GaSb NWs (without S), the blue curve is S-GaSb NWs with S 3.3%, and the red curve is S-GaSb NWs

with S 6.6%. As can be seen from Figure 2a of the Ga 3s spectra, the Ga 3s (160.8 eV) peak is found in the pure GaSb NWs,[28,39] while the peaks of S-GaSb NWs shift to higher binding energy value, which may be due to the S incorporation. In Figure 2b of Ga 3d, the same peaks of Ga−Sb (18.7 eV) bonding and Ga−O (20.3 eV) bonding are found in all of the pure GaSb NWs and S-GaSb NWs through the Gauss−Lorentz fitting. It is indicated that the surface Ga atoms are exposed to the ambient and are prone to be oxidized.[21,25] In Figure 2c, the Sb 4d spectrum of pure GaSb NWs is decomposed into Sb $4d_{3/2}$ (31.5 eV), Sb $4d_{5/2}$ (32.7 eV), Sb−O bindings ($4d_{3/2}$ at 33.9 eV and Sb $4d_{5/2}$ 35.0 eV), and a barely noticeable impurity peak.[21,25] Interestingly, the Sb−O peaks of all the S-GaSb NWs are not detected. Moreover, the Sb−S peaks also do not appear. It is clear that the Sb atoms are protected from exposure to ambient oxygen when the S surface passivator is adopted in the experiment.

In order to verify the surface bonding environment of the S-GaSb NWs, the sample of S-GaSb NWs with S 6.6% is treated by Ar ion etching, which is attached to the XPS equipment. Figure S6 are SEM images of the sample before and after etching 40 s. The XPS spectra are illustrated in Figure 2d−f, which show before and after etching for 40 s and 10 min. In Figure 2d of Ga 3s, the spectrum can be decomposed into the Ga 3s (160.8 eV) and the Ga−S bonding (162.0 eV) peaks before etching.[27,28] After etching 40 s, the Ga−S bonding peak becomes obviously stronger. When the etching time reached 10 min, the Ga−S bonding peak faded away, remaining the main Ga 3s peak. This indicates that the formed Ga−S bonding occurs only in the surface layer instead of being incorporated into the NW core. Simultaneously in Figure 2e of the Ga 3d spectra, with the process of etching, the Ga−O (20.5 eV) bonding peak disappeared gradually, and only the Ga−S (18.9 eV) bonding peak remained.[21,25] Noticeably, the etching has no discernible influence on the sample spectra of Sb 4d in Figure 2f, which is consistent with the result of Figure 2c that the surface Sb atoms are protected from exposure to oxygen and are also not formed from Sb−S bonding.

From the XPS spectra before and after etching, we can deduce the surface structures of pure GaSb NWs and S-GaSb NWs as shown in Figure S7a,b. Because of exposure to the ambient oxygen, the surface of pure GaSb NWs has Ga−O and Sb−O bonding, while the surface of S-GaSb NWs only has Ga−S and Ga−O bonding. With the etching progress, Ga−S and Ga−O bonding of the S-GaSb NWs disappear gradually. It could be ascertained that the S atoms are only on the surface and form a surface passivation layer of Ga_xS_y in the S-GaSb NW, which can prevent the oxidation of Sb in the NW core. To confirm our hypothesis, Figure S7c−g shows the the STEM and EDS element mapping images of the controlled S-GaSb NWs sample that is grown with S 50% in the precursor. It is obvious that the NW consists of the GaSb core and a thick Ga−S surface passivation layer, which further reinforces our conclusion. Our result is in distinct contrast to the formation of Sb−S surface layers in S-catalyzed GaSb NWs reported previously.[22,25] The reason behind this difference probably is that the carrier gas of NWs growth was pure H_2 in previous reports, whereas the carrier gas is N_2/H_2 9:1 in this work. Compared with Sb−S bonding, the Ga−S bonding with higher oxidability is not suppressed and formed preferentially in our experiment.

To evaluate the influence of the surface S-passivation layer on the NW photoresponse properties, NW-devices are
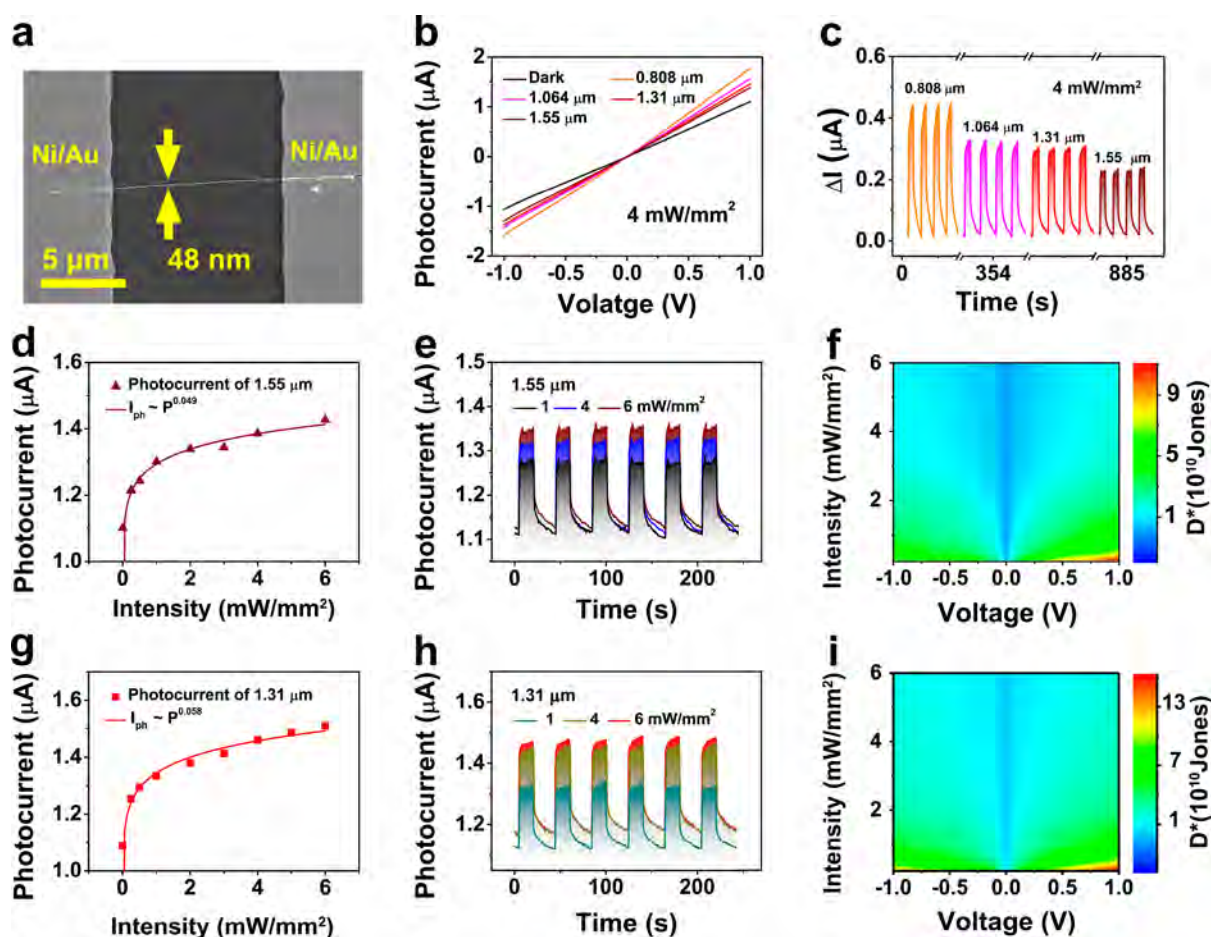
Figure 3. Photoresponse properties for near-infrared light of the S-GaSb NW-based photodetector. (a) SEM image of the photodetector. (b) $I-V$ and (c) $I-T$ curves under various incident light from 0.808 to 1.55 μm. Photoresponse properties for incident 1.55 μm light (d) $I_{ph}-P$ plot and (e) $I-T$ curves, (f) 2D map of the D^* as a function of bias voltage and 1.55 μm light power intensity. Photoresponse properties for incident 1.31 μm light (g) $I_{ph}-P$ plot and (h) $I-T$ curves; (i) 2D map of the D^* as a function of bias voltage and 1.31 μm light power intensity.

constructed with Ni/Au electrodes (10/50 nm) at both ends. Parts g−i of Figure 2 are random statistics of 30 NW devices properties, respectively. Pure GaSb NWs are black histograms, S-GaSb NWs with S 3.3% are blue histograms, and S-GaSb NWs with S 6.6% are red histograms. Figure 2g is the statistical result of dark currents where the normal distribution of pure GaSb NWs is 2.43 ± 0.47 μA, of S-GaSb NWs with S 3.3% is 1.36 ± 0.51 μA, of S-GaSb NWs with S 6.6% is 1.29 ± 0.41 μA. It is apparent that the dark current is reduced with the increasement of S. The infrared photoresponse properties of these devices are studied under the illumination of 1.55 μm light with the intensity of 4 mW/mm^2 at 1 V bias. Figure S8a−c shows typical $I-V$ curves, and Figure S8d is the statistic of I_{ph}/I_{off} which is the ratio of the photocurrent to the dark current. From the statistical results of I_{ph}/I_{off} ratios, all-component NWs devices have the similar value. However, the NW devices of S-GaSb NWs with S 6.6% have the lowest dark currents implying that they would possess the higher responsivity (R_λ) and detectivity (D^*) values. The R_λ and D^* are key parameters for the photodetector, which could be calculated by the following equation[16,40−46]

$$R_\lambda = \frac{\Delta I}{(PS)} = \frac{I_{photo} - I_{dark}}{PS} \tag{1}$$

$$D^* = R_\lambda \left(\frac{SB}{2eI_{dark}} \right)^{1/2} \tag{2}$$

where P is the power intensity of incident light, S is the effective illumination area, B is the bandwidth, and e is the elementary electronic charge. The statistical results of R_λ and D^* are presented in Figure 2h,i. The normal distributions are 62.5 ± 22.5 A/W and $(9.36 \pm 3.00) \times 10^9$ Jones for pure GaSb NWs, 101.7 ± 51.4 A/W and $(1.22 \pm 0.48) \times 10^{10}$ Jones for S-GaSb NWs with S 3.3%, and 134.7 ± 51.4 A/W and $(1.31 \pm 0.48) \times 10^{10}$ Jones for S-GaSb NWs with S 6.6%, respectively. The R_λ and D^* values of pure GaSb NWs is consistent with our previous report and other studies.[22,23] It is obvious that the R_λ and D^* of S-GaSb NWs are elevated due to the S surface passivation, and S-GaSb NWs with S 6.6% have best photoresponse properties. Thus, S-GaSb NWs with S 6.6% are selected and thoroughly studied in subsequent sections.

Single FET/photodetectors based on the S-GaSb NW with S 6.6% are discussed in detail. The device is constructed on the Si/SiO$_2$ substrate as introduced in the Experimental Section. Figure S9a shows the schematic illustration of the device. The back gate is monocrystalline (100) Si, and the dielectric layer is 300 nm SiO$_2$. Owing to p-type properties of the GaSb, the Ni/Au (10/50 nm) are used as electrodes to build ohmic contacts.

The SEM image of the S-GaSb NW-based FET/photodetector is presented in Figure 3a; the diameter of the S-GaSb NW is 48 nm, and the device channel is 10 μm. The field-effect transistor (FET) properties of the device are demonstrated in Figure S9b−d. A typical p-type transfer behavior could be observed in Figure S9b, which affirms that it is the p-type semiconductor. The device also reveals well output characteristics in Figure S9c. As shown in Figure S9d, the peak value of hole mobility μ_h is calculated to be 48.9 cm^2 V^{-1} s^{-1}. Although the S-GaSb NW-based device has good FET performances, it does not achieve the best properties as in the previous report.[25,29] The reason may be attributed to the influence of the surface S-passivation layer which can hinder the transfer of carriers from the NW to the electrode. However, when the S-GaSb NW is built as a photodetector, the surface S-passivation layer can reduce the dark current. According to eqs 1 and 2, the lower dark current is beneficial to enhance photoresponse properties. In this work, photoresponse properties of the S-GaSb NW-based photodetector are studied in detail.

All of the photoresponse measurements are conducted in an open atmosphere at room temperature. In Figure 3b, the I−V curves of the S-GaSb NW-based photodetector are tested under the illumination of near-infrared monochromatic light from 0.808 to 1.55 μm. The schematic illustration is depicted in Figure S10a. The power intensity of incident light is calibrated as 4 mW/mm^2. From these I−V curves, it is apparent that the photocurrent has been elevated compared with the dark current. In Figure 2c, the photocurrent versus time (I−T) curves are recorded at 1 V bias by turning the light on and off. The photocurrent increases to the saturated state ("on") when the light shines and then recovers the original state ("off") when the light turns off periodically. The good reproducibility and stability of the I−T curves manifest well the photoresponse properties to near-infrared light from 0.808 to 1.55 μm. The photoresponse performances of the S-GaSb NW-based photodetector for communication wavelengths of 1.55 and 1.31 μm are investigated systematically. In Figure 3d, under the illumination of 1.55 μm light, it is found that the increase of photocurrent is slowed gradually with the enhancement of light power intensity. Their relationship can be fitted by a power law of $I_{ph} \sim P^{0.049}$ where I_{ph} is the photocurrent and P is the light power intensity. Figure 3e shows the I−T curves of the device, at 1 V bias, under irradiation of 1.55 μm light with various power intensities of 1, 4, and 6 mW/mm^2. These I−T curves also increase to the "on" state and recover to the "off" state with the light turning on and off periodically. For 1.31 μm incident light, the relationship of photocurrent and power intensity could be fitted as $I_{Ph} \sim P^{0.058}$ in Figure 3g, which is similar to that of 1.55 μm light. In Figure 3h, I−T curves for incident 1.31 μm light are also similar to that of 1.55 μm light. Defined as an increase from 10% to 90% of the I−T curve, the response time is measured by the fast test model of our equipment.[22,47] As drawn in Figure S10b,c, the response time is 0.05 s for 1.55 μm light and 0.1 s for 1.31 μm light. The responsivity (R_λ) and detectivity (D^*) are vital parameters for the photodetector, which could be calculated by the aforementioned eqs 1 and 2. Figure S10d expresses the 2D mapping of the calculated R_λ as a function of bias voltage and 1.55 μm power intensity, and Figure 3f is the 2D mapping of the calculated D^* as a function of bias voltage and 1.55 μm power intensity. At specific voltage bias, it can be recognized that the higher values of R_λ and D^* are obtained under the incident light with lower power intensity. The reason is

ascribed to the nonlinear relationship between the photocurrent and the light power intensity fitted as $I_{ph} \sim P^{0.049}$ in Figure 3f, where there is a bigger slope in the lower power region. The analogous phenomena in 2D mappings of R_λ and D^* for 1.31 μm light are illustrated in Figure S10e and Figure 3i. The calculated value of R_λ and D^* of the photodetector for 1.55 μm light are summarized in Table S1 and for 1.31 μm light are summarized in Table S2. It can be seen clearly that all R_λ are higher than 10^2 A/W and all D^* are higher than 10^{10} Jones. Under the lowest power intensity of 0.25 mW/mm^2, at 1 V bias, the maximum R_λ and D^* can be achieved, which is 9.39 × 10^2 A/W and 1.10 × 10^{11} Jones for 1.55 μm light and 1.38 × 10^3 A/W and 1.61 × 10^{11} Jones for 1.31 μm light. Under common conditions, 1 mW/mm^2 power intensity, and 1 V bias, the R_λ and D^* are 4.15 × 10^2 A/W and 4.84 × 10^{10} for 1.55 μm light and 5.13 × 10^2 A/W and 6.02 × 10^{10} Jones for 1.31 μm light. These R_λ values are higher than 77.3 A/W for the pure GaSb NW photodetector in our previous work and 61 A/W of Sn-doped GaSb NW photodetector in other reports.[22,23]

The noise equivalent power (NEP) is known as another key parameter for the photodetector, which actually reflects the lowest light power that a photodetector can respond to when the signal-to-noise ratio is 1. The NEP can be calculated by the following equation[40,48]

$$INC = \frac{\int_0^B sid(f)\,df}{\sqrt{B}} = \frac{I_{in}}{\sqrt{B}} \qquad (3)$$

$$NEP = \frac{INC}{R_\lambda} \qquad (4)$$

where INC is the integration of noise current, $sid(f)$ is the function of noise current, f is the frequency, I_{in} is the equivalent current noise and B is the bandwidth. The INC of the S-GaSb NW-based photodetector can be measured directly in our laboratory as shown in Figure S10f. The calculated NEP of the photodetector is demonstrated in Figure S10g. The commercial Si photodetector (Newport, model 1601, user's manual) has an NEP of 16 pW/(Hz)$^{1/2}$ in 30 kHz. The near-infrared InGaAs photodetector (Newport, model 1611, user's manual) has an NEP of 20 pW/(Hz)$^{1/2}$ in 30 kHz. However, the NEP of our photodetector for 1.55 μm light is less than 1 pW/(Hz)$^{1/2}$ in the same frequency range. It is obviously lower than that of the above commercial photodetectors, manifesting the good near-infrared photoresponse properties of our S-GaSb NW-based photodetector.

As is well-known, the NW photodetector possesses an intrinsic anisotropy photoresponse for linear polarization light, which is wavelength-independent as long as the energy of light larger than the NW band gap.[12,13,23,49] The polarized photoresponse of the S-GaSb NW-based photodetector is investigated in this work. The device photograph is demonstrated in Figure S11a corresponding to the SEM image of Figure 3a. The light beam is vertically irradiating on the device through the Glan-Taylor prism, and the half-wave plate in turns as plotted in Figure S11b. The power intensity of linear polarization light is fixed at 1.34 mW/mm^2, and the initial angle is parallel to the S-GaSb NW long-axis which is defined as 0°. The half-wave plate is rotated with a step of 10° which results in the incident polarization light rotated with a step of 20°. The currents are measured under linear polarization light of 0.808, 1.064, 1.31, and 1.55 μm. To
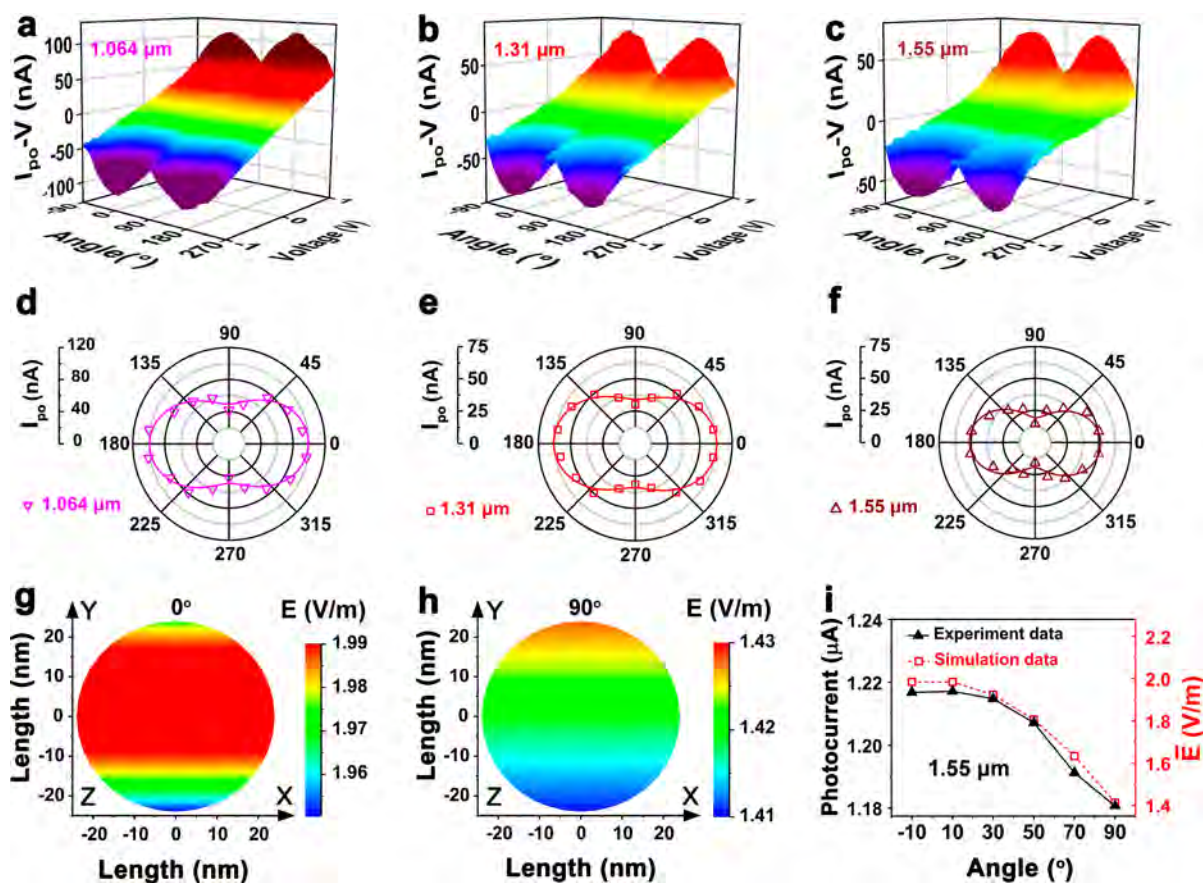
Figure 4. Polarized photoresponses of the S-GaSb NW-based photodetector. (a−c) 3D surface maps of polarized photocurrent I_{po} (z-axis) versus V_d (x-axis) and polarized angle (y-axis) for incident linear polarization light of 1.064, 1.31, and 1.55 μm. (d−f) Evolution of the I_{po} with the polarized angle of 1.064, 1.31, and 1.55 μm light, respectively, at 1 V bias. (g−h) Calculated intensity maps of light electric field E inside the NW under perpendicular (90°) and parallel (0°) 1.55 μm light. (i) The average of calculated E intensity inside the NW (dash line) and the measured photocurrent (solid line) as a function of polarized angles of incident 1.55 μm light.

better elucidate the photoresponse anisotropy, the polarized photocurrent I_{po} is defined as[11,50]

$$I_{po} = I_{ph}(\theta) - I_{dark} \qquad (5)$$

The $I_{po}-V$ curves of the device under the illumination of polarized 0.808, 1.064, 1.31, and 1.55 μm light are shown in Figure S11c and Figure 4a−c, respectively. Strong polarized photoresponse is observed apparently, which confirms that the S-GaSb NW-based photodetector could clearly identify the polarized direction of incident light. Notably, when the incident linear polarization light is paralleled to the NW long-axis (0°, 180°) the maximum value of I_{po} could be achieved, and when is perpendicular to NW long-axis (90°, 270°) the minimum value of I_{po} is recorded. The evolution of the I_{po} at 1 V bias is further extracted as a function of polarized angle in the polar coordinate as illustrated in Figure S11d and Figure 4d−f. The variation law of I_{po} could be fitted by the following equation[7,11,23,50]

$$I_{po}(\theta) = I_{pox} \cos^2(\theta + \varphi) + I_{poy} \sin^2(\theta + \varphi) \qquad (6)$$

where θ is the variable angle of linear polarization light with respect to the reference direction 0° and φ is a fixed angle. $I_{po}(\theta)$, I_{pox}, and I_{poy} are the theoretical components of I_{po} along θ, x-axis and y-axis directions. Through measurement results, the dichroic ratio (I_{poy}/I_{pox}) is 2.35 under 0.808 μm light, 2.00 under 1.064 μm light, 1.85 under 1.31 μm light, and 2.65

under 1.55 μm light, respectively. These dichroic ratios are higher than 1.84 of 2D NbS$_3$ under 0.83 μm light, 1.2 of 2D GeSe under 1.31 μm light, and 2.39 of quasi-2D Te under 1.55 μm light in recent reports.[5,6,51]

The polarized photoresponse of S-GaSb NW-based photodetector is originated from the attenuation of light electric field intensity inside the NW under linear polarization light with different direction.[12,13,15,49] For the well-isolated NW, there is a large dielectric contrast between the NW and the surrounding air. Because the wavelength of incident light is much larger than the NW diameter, the NW could be regarded as a cylinder with infinite dielectric in air. When the electric field component of incident light is parallel to the NW long-axis, the light electric field (E) inside the NW is not diminished. However, when perpendicular to the long-axis, the light electric field (E) inside the NW could be attenuated.[12,13,49] To verify this theory, a COMSOL simulation is conducted. As shown in Figure S12, the NW model is built according to the SEM image in Figure 3a where the diameter of S-GaSb NW is 48 nm and the length of the NW is 10 μm. The linear polarization light of 1.55 μm is used as external exciting light source. The light power received on the NW surface is 10 nW equal to 1.33 mW/mm^2, which is almost equal to the 1.34 mW/mm^2 of incident polarization light used in this experiment. The background electric field is 1 V/m. In Figure S12a, there is the apparent E distribution inside the NW body under the parallel polarization (0°) light, while
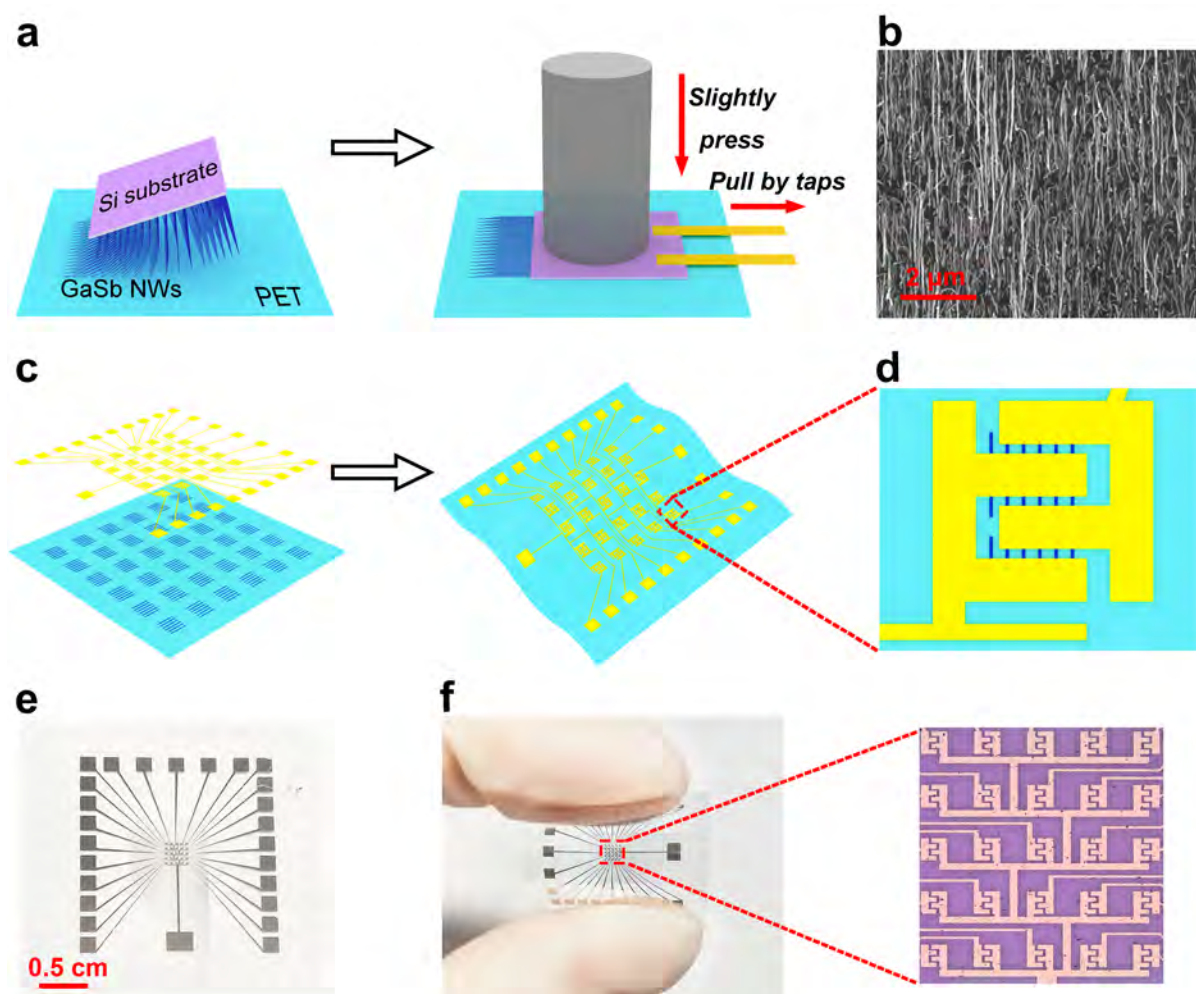
Figure 5. Fabrication of the flexible polarimetric image sensor based on ordered S-GaSb NW arrays. (a) Schematic illustration of the contact printing process for ordered S-GaSb NWs arrays. (b) SEM image of the ordered S-GaSb NWs arrays on the flexible PET substrate. (c) Layer architecture of the flexible polarimetric image sensor. (d) Schematic illustration of one pixel of the sensor. (e) Photograph of the flexible polarimetric image sensor. (f) Photograph of the 5 × 5 pixels structure of the flexible polarimetric image sensor.

in Figure S12b the E distribution inside the NW body is obviously attenuated under the perpendicular polarization (90°) light. Figure 4g,h is the E distribution in a $X-Y$ plane where Z position is 50 μm middle of the NW long-axis. It is more clearly that the E intensity inside the NW under the 0° polarized 1.55 μm light is much stronger than that of under the 90° polarized 1.55 μm light. In Figure S12c, the average of the E intensity inside the NW is calculated under different angle polarization 1.55 μm light from $-10°$ to $+90°$ with a step of 10°. It is evident that the average of E intensity is decreased gradually with the increase of polarized angles. As is well-known, light electric field (E) intensity is proportional to the light power intensity P. From the law of $I_{ph} \sim P^{0.049}$ in Figure 3d, the photocurrent I_{ph} and the P are approximately proportional relationship near P = 1.33 mW/mm^2, which is the power intensity of external exciting light in the COMSOL simulation. This means that the E intensity is almost proportional to the photocurrent I_{ph}. A higher E intensity inside the NW could produce a greater photocurrent I_{ph}. Figure 4i illustrates the average of calculated E inside the NW and the measured I_{ph} as a function of the polarized angle of incident 1.55 μm light. Both calculated E and measured I_{ph} have a similar decrease tendency with the polarized angle

rotated. This result is consistent with our analysis and confirms the theory that there is an attenuation of the light electric field E intensity inside the NW under different directions of polarization light.

With characteristics of anisotropy, directionality, uniformity, and programmability, ordered NWs arrays have shown potential applications in modern nanodevices.[18] As summarized in Table S3, they have been exploited as strain sensors, photodetectors, polarized photoluminescence, MOSFET devices, and even logic circuits.[52−56] However, there are rare reports about the application of polarimetric image sensors based on ordered NW arrays. In this work, it can be inferred that ordered S-GaSb NWs arrays would have the potential for integrating flexible polarimetric image sensors due to the polarized photoresponse performances of single S-GaSb NW. There are many methods for the assembly of ordered NWs arrays such as fluid flow directed assembly, contact printing, differential roll printing, electric/magnetic-field-assisted assembly, Langmuir−Blodgett assembly, and so on.[17,18,56−60] Among these methods, contact printing is one of most convenient and effective ways.[58,60] As in our previous report, Figure 5a depicts the preparation procedure of ordered S-GaSb NWs arrays by the contact printing.[60,61] The Si substrate grown with high
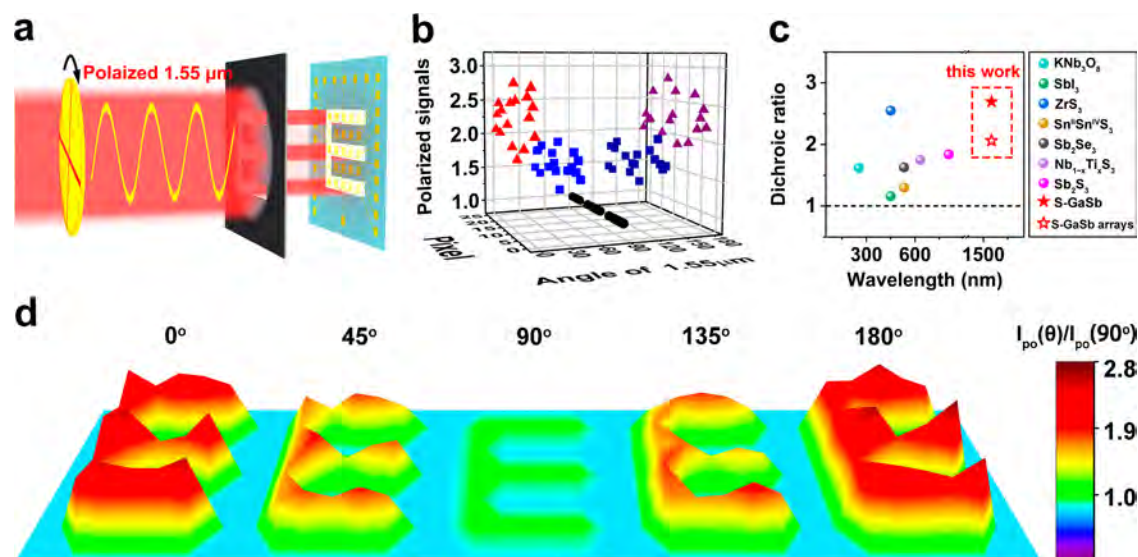
Figure 6. Polarization imaging capability of the flexible polarimetric image sensor based on ordered S-GaSb NWs arrays. (a) Schematic illustration of the flexible image sensor under polarized 1.55 μm light with an "E" mask and (b) polarized signals normalized by $I_{po}(\theta)/I_{po}(90°)$ of each pixel under various angle polarized 1.55 μm light with the "E" mask. (c) Dichroic ratio comparison between single S-GaSb NW, ordered S-GaSb NWs array polarization photodetectors (this work), and other reported 1D polarization photodetectors. (d) Output 3D images of the polarimetric image sensor corresponding to the mask "E".

density S-GaSb NWs is upside-down on the flexible PET receiver substrate. The Si substrate is pressed slightly, while it slides rapidly under a pull of tapes. The as-grown NWs will be detached from the Si substrate and combed by the shear force. Attributed to the effect of van der Waals force, the NWs can be adhered tightly to the receiver substrate and form ordered arrays. Figure 5b is the SEM image of ordered S-GaSb NWs arrays on the flexible PET substrate where the NWs are arranged in a well orderly direction. Figure 5c depicts the fabrication procedure of the flexible polarimetric image sensor based on ordered S-GaSb NWs arrays. A 5 × 5 pixel image sensor is constructed on the top of NW arrays through standard photolithography, thermal evaporation, and lift-off processes.[42] A schematic illustration of one pixel of the sensor is illustrated in Figure 5d. Figure 5e is the photograph of the fabricated flexible polarimetric image sensor on the PET substrate. The detailed structure of the image sensor is depicted in Figure 5f. The image sensor has 5 × 5 pixel photodetectors, and each pixel with two interdigital electrodes is connected by side electrodes.[62,63] The polarized photoelectric signals of each pixel can be collected by external circuits. Photographs of pixels are illustrated in Figure S13. Figure S13b−d shows high-magnification photographs corresponding to the pixels in Figure S13a. The effective channel length is 10 μm, and it is obvious that there are distributions of ordered S-GaSb NW arrays in the channel of each pixel. The polarized photoresponse properties of these pixels are exhibited in Figure S13e,f. Under the polarized 1.55 μm light with 1.34 mW/mm^2 intensity, the dichroic ratio of the pixel in Figure S13b is 2.04, of the pixel in Figure S13c is 1.93, and of the pixel in Figure S13d is 1.89. These high dichroic ratios confirm the well near-infrared polarization photoresponse performances of our prepared flexible polarimetric image sensor based on ordered S-GaSb NW arrays.

The polarized imaging capability of our flexible polarimetric image sensor is investigated in Figure 6. As shown in Figure 6a, a hollow mask of "E" is placed in front of the image sensor. The linear polarization 1.55 μm light through the mask formed

a "E" pattern polarization light source. The pixels will be illuminated in the corresponding "E" area, and others are dark. When the "E" pattern has a 90° polarized angle, the $I_{po}(90°)$ are recorded first, and then the half-wave plate is rotated to change the polarization angles and $I_{po}(0°)$, $I_{po}(45°)$, $I_{po}(135°)$, and $I_{po}(180°)$ are recorded later. Figure 6b presents polarized signals normalized with $I_{po}(\theta)/I_{po}(90°)$. Consistent with polarized photoresponse performances of the single S-GaSb NW, the polarized signals of each pixel reach a maximum under the "E" pattern with 0° and 180°, which are parallel to ordered S-GaSb NWs arrays inside the pixel and down to a minimum under the "E" pattern at 90°, which is perpendicular. Figure 6c is the summary of dichroic ratios of single S-GaSb NW, ordered S-GaSb NW array polarization photodetectors in this work, and other reported 1D or quasi-1D polarization photodetectors in previous reports. Both single S-GaSb NW and ordered S-GaSb NWs arrays possess better polarization-sensitive performances than the majority of reported KNb$_3$O$_8$,[64] SbI$_3$,[65] ZrS$_3$,[66] Sn^{II}Sn^{IV}S$_3$,[67] Sb$_2$Se$_3$,[68] Nb$_{1-x}$Ti$_x$S$_3$,[69] Sb$_2$S$_3$,[7] etc. The obtained data are exhibited in Table S4. The final output 3D images of the "E" pattern are illustrated in Figure 6d. The "E" image with 0° (180°) is apparently stronger than the "E" images with 90° and 45° (135°). "T" and "C" masks are utilized as polarized 1.55 μm light sources, which are also explored in this work. The output 2D images of "E", "T", and "C" are displayed in Figure S14 where the images with a 0° (180°) are bright, and the images with 90° and 45° (135°) are ambiguous. These obvious brightness contrasts manifest the superior near-infrared polarization imaging ability of our flexible polarimetric image sensor based on ordered S-GaSb NW arrays.[17,70,71]

CONCLUSIONS

In summary, through the S-catalyzed method, S-GaSb NWs are grown successfully in a conventional CVD system. When the mass percentage of S is 6.6% in the precursor, the as-grown S-GaSb NWs have a thinner diameter. Through the HRTEM

and XPS analysis, it can be confirmed that a surface passivation layer of Ga_xS_y is formed on the NW surface. The photodetector based on the S-GaSb NW exhibits large responsivity values of 9.39×10^2 and 1.38×10^3 A/W and ultrahigh detectivities of 1.10×10^{11} and 1.61×10^{11} Jones for near-infrared 1.55 and 1.31 μm light. Simultaneously, the device also demonstrates polarization photoresponse performances, with dichroic ratios of 2.65 and 1.85 under polarized 1.55 and 1.31 μm light. Through a COMSOL simulation, the polarized photoresponse is ascertained to the attenuation of light electric field intensity inside the NW when the polarized angle of incident light rotates. What's more, ordered S-GaSb NWs arrays are fabricated by the contact printing method. A flexible polarimetric image sensor is constructed on the ordered NWs arrays, which reveals superior polarization imaging ability for incident polarization 1.55 μm light. The ordered S-GaSb NWs arrays are promising for the next-generation flexible polarimetric imaging sensors because of their lightweight, portable, and low cost feauers, which are vital for the development of communication exchange, biological diagnosis, and optical engineering.

EXPERIMENTAL SECTION

Synthesis of Sulfur-Passivation GaSb Nanowires. The sulfur-passivation GaSb (S-GaSb) NWs were synthesized via a horizontal quartz tube furnace with two heating zone as illustrated in Figure S1. Commercially available GaSb powers and S powers, as the solid source, were placed in the center of the first heating zone. A (100) Si wafer coated with 3 nm Au film, as the growth substrate, was placed in the center of the second heating zone. In order to achieve the best surface-passivated results, different mass ratios between S powers and GaSb powers were adopted in this experiment. The mass of the GaSb powers was constant at 0.3 g. The masses of the S powers were 0, 0.01, 0.02, and 0.3 g, respectively, which meant that the mass percentages of the S were 0%, 3.3%, 6.6%, and 50%, in the precursor. The subsequent growth conditions, including temperature and pressure, were carefully controlled to harvest high-quality nanowires. The furnace was first evacuated down to 1×10^{-3} Torr to remove the air. Then the carrier gas, N_2/H_2 (volume ratio 9:1), was flowed into the quartz tube with a constant flux, and the quartz tube maintained a constant pressure. The first heating zone and second heating zone were heated to 750 and 550 °C in 10 min, respectively. The pressure and temperature states were kept for a duration of 60 min. They were cooled to room temperature, and the abundant nanowires were found to deposit on the whole Si substrate.

Characterization Methods. The morphology and crystallographic structure of the nanowires were characterized by SEM (Hitachi S4800) and CS corrected HRTEM (JEOL ARM200F). The chemical composition and elemental valence were analyzed by XRD (D8 ADVANCE, Bruker) and XPS (Escalab 250Xi, Thermo). The microphotoluminescence (PL) was detected using an iHR320 infrared spectrometer, and the PL signal was excited using an 800 nm laser (pulse width 20 ps, repetition frequency 80 MHz) with a power of 2 mW.

Device Fabrication. The single S-GaSb NW photodetector was fabricated on a rigid SiO_2 substrate, and the ordered S-GaSb NWs arrays photodetectors were fabricated on flexible PET substrate. The construction of the devices was as follows. By means of the contact printing, a single S-GaSb NW was transferred to a Si/SiO_2 substrate, and ordered S-GaSb NW arrays were transferred to a flexible PET substrate. The patterns of electrodes (Ni/Au 10/50 nm) were fabricated by standard photolithography, thermal evaporation, and lift-off processes. The photodetector based on a single S-GaSb NW and a flexible polarimetric image sensor based on ordered S-GaSb NW arrays were completed.

Electronic and Optoelectronic Measurements. The electric and photoelectric signals of the single S-GaSb NW photodetector were measured on a Keithley B1500A semiconductor characterization system connected to a probe station. The light sources were the semiconductor lasers, 0.808 μm (CNI, MDL-III-808), 1.064 μm (CNI, MDL-III-1064), 1.31 μm (CNI, MDL-III-1310), and 1.55 μm (CNI, MDL-III-1550). The laser was directly illuminated on the photodetector without focusing, and the diameter of the laser spot was measured as 2.5 mm in radius. The Newport power meter was employed to test the power density of the incident laser. The noise power spectra (NEP) were measured by a PDA (Platform Design Automation, Inc.). All of the measurements were conducted in open atmosphere at room temperature.

Polarized Photocurrent Measurements. The polarized properties of the single S-GaSb NW photodetector and flexible polarimetric image sensor were tested using our homemade optical path system that consisted of a polarizer (Glan-Taylor prism), a half-wave plate, and a vertical sample stage for device placement which could connect to the Keithley B1500A semiconductor characterization system. The polarized direction of the incident light was modulated by the polarizer and half-wave plate before irradiation of the devices. The light sources were also the aforementioned semiconductor lasers at 0.808, 1.064, 1.31, and 1.55 μm. The power intensity of the incident polarization light was fixed at 1.34 mw/mm², and the radius was 3 mm. All of the measurements were also conducted in open atmosphere at room temperature.

Numerical Simulation. The numerical simulation was performed using the commercial software COMSOL Multiphysics 5.4. The model of the NW was built according to the SEM image of the S-GaSb NW in Figure 3a. An isolated GaSb NW with diameter 48 nm and length 10 μm was built in a vacuum. The linear polarization light of 1.55 μm was used as external exciting source to illuminate the NW from the top. The power of incident linear polarization light was 10 nW on the NW surface, equivalent to 1.33 mW/mm². The direction of the incident linear polarization light was rotated from −10° to +90° along the long axis of the NW with a step of 10°. The background electric field was 1 V/m. In order to simulate the real experimental conditions, a bias of 1 V was also added between the NW two side. The distribution of the light electric field inside the NW was calculated under the illumination of the aforementioned linear polarization light with different directions.

ASSOCIATED CONTENT

Ⓢ **Supporting Information**

The Supporting Information is available free of charge at https://pubs.acs.org/doi/10.1021/acsnano.2c01455.

> Synthesized process of S-GaSb NWs, SEM images of large areas of as-grown S-GaSb NWs, PL analysis of as-grown S-GaSb NWs, EDS element mapping of S-GaSb NWs with S 6.6%, XPS spectra of C 1s and S 2s of as-grown S-GaSb NWs, SEM images of S-GaSb NWs with S 6.6% before and after etching 40 s with Ar ions, schematic illustration of the surface structure of S-GaSb NWs with S 50%, typical $I-V$ curves of photodetectors based on pure GaSb NW, S-GaSb NW with S 3.3%, and S-GaSb NW with S 6.6%, FET properties of the S-GaSb NW-based device, near-infrared photoresponse performances of the S-GaSb NW-based photodetector, polarized photoresponses of the S-GaSb NW-based photodetector, COMSOL simulation of light electric field E inside the S-GaSb NW under 1.55 μm linear polarization light, photograph of the flexible polarimetric image sensor based on ordered S-GaSb NWs arrays and its polarized photoresponse property, output 2D images of the polarimetric images sensor corresponding to "E", "T", and "C" masks, summary of the R_λ and D^* of the S-GaSb NW-based photodetector for 1.55 μm light (Table S1), summary of the R_λ and D^* of the S-GaSb NW-

based photodetector for 1.31 μm light (Table S2), summary of typical researches of the ordered NWs arrays in recent reports (Table S3), dichroic ratio comparison between polarized photodetectors in this work and other 1D or quasi-1D polarized photo-detectors in previous reports (Table S4) (PDF)

AUTHOR INFORMATION

Corresponding Authors

Yubao Li − *Hebei Key Lab of Optic-electronic Information and Materials, the College of Physics Science and Technology, Hebei University, Baoding 071002, China;* ⬤ orcid.org/0000-0002-0979-8747; Email: liyubao@hbu.edu.cn

Johnny C. Ho − *Department of Materials Science and Engineering, and State Key Laboratory of Terahertz and Millimeter Waves, City University of Hong Kong, Hong Kong 999077, China;* ⬤ orcid.org/0000-0003-3000-8794; Email: johnnyho@cityu.edu.hk

Zhongming Wei − *State Key Laboratory of Superlattices and Microstructures, Institute of Semiconductors, Chinese Academy of Sciences, Beijing 100083, China;* ⬤ orcid.org/0000-0002-6237-0993; Email: zmwei@semi.ac.cn

Guozhen Shen − *State Key Laboratory of Superlattices and Microstructures, Institute of Semiconductors, Chinese Academy of Sciences, Beijing 100083, China; School of Integrated Circuits and Electronics, Beijing Institute of Technology, Beijing 100081, China;* ⬤ orcid.org/0000-0002-9755-1647; Email: gzshen@semi.ac.cn

Authors

Kai Zhang − *Hebei Key Lab of Optic-electronic Information and Materials, the College of Physics Science and Technology, Hebei University, Baoding 071002, China; Institute of Physics, Chinese Academy of Sciences and University of Chinese Academy of Sciences, Beijing 100190, China*

Zhihui Ren − *State Key Laboratory of Superlattices and Microstructures, Institute of Semiconductors, Chinese Academy of Sciences, Beijing 100083, China; Centre for Quantum Physics, Key Laboratory of Advanced Optoelxsectronic Quantum Architecture and Measurement (MOE), School of Physics, Beijing Institute of Technology, Beijing 100081, China*

Huichen Cao − *Hebei Key Lab of Optic-electronic Information and Materials, the College of Physics Science and Technology, Hebei University, Baoding 071002, China*

Lingling Li − *State Key Laboratory of Superlattices and Microstructures, Institute of Semiconductors, Chinese Academy of Sciences, Beijing 100083, China*

Ying Wang − *Hebei Key Lab of Optic-electronic Information and Materials, the College of Physics Science and Technology, Hebei University, Baoding 071002, China*

Wei Zhang − *Hebei Key Lab of Optic-electronic Information and Materials, the College of Physics Science and Technology, Hebei University, Baoding 071002, China*

Haitao Yang − *State Key Laboratory of Superlattices and Microstructures, Institute of Semiconductors, Chinese Academy of Sciences, Beijing 100083, China*

You Meng − *Department of Materials Science and Engineering, and State Key Laboratory of Terahertz and Millimeter Waves, City University of Hong Kong, Hong Kong 999077, China*

Complete contact information is available at:

https://pubs.acs.org/10.1021/acsnano.2c01455

Author Contributions

‡K.Z. and Z.H.R. contributed equally to this work. H.C.C. and W.Z. carried out the SEM and TEM measurements. Y.W. carried out the XRD and PL measurements. L.L.L. and Y.M. performed the COMSOL simulation. H.T.Y. guided the analysis of crystal structure. The paper was cowritten by K.Z. and Z.H.R. Y.B.L., J.C.H., Z.M.W., and G.Z.S. guided the whole project.

Notes

The authors declare no competing financial interest.

REFERENCES

(1) Tyo, J. S.; Goldstein, D. L.; Chenault, D. B.; Shaw, J. A. Review of passive imaging polarimetry for remote sensing applications. *Appl. Opt.* **2006**, *45*, 5453−5469.

(2) Fingas, M.; Brown, C. E. A Review of Oil Spill Remote Sensing. *Sensors (Basel)* **2018**, *18*, 91.

(3) Zheng, C.; Zhao, G.; Liu, W.; Chen, Y.; Zhang, Z.; Jin, L.; Xu, Y.; Kuang, C.; Liu, X. Three-dimensional super-resolved live cell imaging through polarized multi-angle TIRF. *Opt. Lett.* **2018**, *43*, 1423−1426.

(4) Wang, X.; Xiong, T.; Zhao, K.; Zhou, Z.; Xin, K.; Deng, H. X.; Kang, J.; Yang, J.; Liu, Y. Y.; Wei, Z. Polarimetric Image Sensor and Fermi Level Shifting Induced Multichannel Transition Based on 2D PdPS. *Adv. Mater.* **2022**, *34*, 2107206.

(5) Wang, Y.; Wu, P.; Wang, Z.; Luo, M.; Zhong, F.; Ge, X.; Zhang, K.; Peng, M.; Ye, Y.; Li, Q.; Ge, H.; Ye, J.; He, T.; Chen, Y.; Xu, T.; Yu, C.; Wang, Y.; Hu, Z.; Zhou, X.; Shan, C.; Long, M.; Wang, P.; Zhou, P.; Hu, W. Air-Stable Low-Symmetry Narrow-Bandgap 2D Sulfide Niobium for Polarization Photodetection. *Adv. Mater.* **2020**, *32*, 2005037.

(6) Tong, L.; Huang, X.; Wang, P.; Ye, L.; Peng, M.; An, L.; Sun, Q.; Zhang, Y.; Yang, G.; Li, Z.; Zhong, F.; Wang, F.; Wang, Y.; Motlag, M.; Wu, W.; Cheng, G. J.; Hu, W. Stable mid-infrared polarization imaging based on quasi-2D tellurium at room temperature. *Nat. Commun.* **2020**, *11*, 2308.

(7) Zhao, K.; Yang, J.; Zhong, M.; Gao, Q.; Wang, Y.; Wang, X.; Shen, W.; Hu, C.; Wang, K.; Shen, G.; Li, M.; Wang, J.; Hu, W.; Wei, Z. Direct Polarimetric Image Sensor and Wide Spectral Response Based on Quasi-1D Sb$_2$S$_3$ Nanowire. *Adv. Funct. Mater.* **2021**, *31*, 2006601.

(8) Zhou, Z.; Long, M.; Pan, L.; Wang, X.; Zhong, M.; Blei, M.; Wang, J.; Fang, J.; Tongay, S.; Hu, W.; Li, J.; Wei, Z. Perpendicular Optical Reversal of the Linear Dichroism and Polarized Photo-detection in 2D GeAs. *ACS Nano* **2018**, *12*, 12416−12423.

(9) Venuthurumilli, P. K.; Ye, P. D.; Xu, X. Plasmonic Resonance Enhanced Polarization-Sensitive Photodetection by Black Phosphorus in Near Infrared. *ACS Nano* **2018**, *12*, 4861−4867.

(10) Long, M. S.; Gao, A. Y.; Wang, P.; Xia, H.; Ott, C.; Pan, C.; Fu, Y. J.; Liu, E.; Chen, X. S.; Lu, W.; Nilges, T.; Xu, J. B.; Wang, X. M.; Hu, W. D.; Miao, F. Room temperature high-detectivity mid-infrared

photodetectors based on black arsenic phosphorus. *Sci. Adv.* **2017**, *3*, No. e1700589.

(11) Wang, X.; Li, Y.; Huang, L.; Jiang, X. W.; Jiang, L.; Dong, H.; Wei, Z.; Li, J.; Hu, W. Short-Wave Near-Infrared Linear Dichroism of Two-Dimensional Germanium Selenide. *J. Am. Chem. Soc.* **2017**, *139*, 14976−14982.

(12) Liu, Z.; Chen, G.; Liang, B.; Yu, G.; Huang, H. T.; Chen, D.; Shen, G. Z. Fabrication of high-quality ZnTe nanowires toward high-performance rigid/flexible visible light photodetectors. *Opt. Express* **2013**, *21*, 7799−7810.

(13) Wang, J. F.; Gudiksen, M. S.; Duan, X. F.; Cui, Y.; Lieber, C. M. Highly Polarized Photoluminescence and Photodetection from Single Indium Phosphide Nanowires. *Science* **2001**, *293*, 1455−1457.

(14) del Alamo, J. A. Nanometre-scale electronics with III-V compound semiconductors. *Nature* **2011**, *479*, 317−323.

(15) Casadei, A.; Llado, E. A.; Amaduzzi, F.; Russo-Averchi, E.; Ruffer, D.; Heiss, M.; Dal Negro, L.; Fontcuberta i Morral, A. Polarization response of nanowires a la carte. *Sci. Rep* **2015**, *5*, 7651.

(16) Wang, J. J.; Fu, C.; Cheng, H. Y.; Tong, X. W.; Zhang, Z. X.; Wu, D.; Chen, L. M.; Liang, F. X.; Luo, L. B. Leaky Mode Resonance-Induced Sensitive Ultraviolet Photodetector Composed of Graphene/Small Diameter Silicon Nanowire Array Heterojunctions. *ACS Nano* **2021**, *15*, 16729−16737.

(17) Jia, C.; Lin, Z.; Huang, Y.; Duan, X. Nanowire Electronics: From Nanoscale to Macroscale. *Chem. Rev.* **2019**, *119*, 9074−9135.

(18) Wang, R.; Chen, C.; Zheng, Y.; Wang, H.; Liu, J.-W.; Yu, S.-H. Structure-property relationship of assembled nanowire materials. *Mater. Chem. Front.* **2020**, *4*, 2881−2903.

(19) Gogler, S.; Bieszczad, G.; Swiderski, J.; Firmanty, K.; Barela, J.; Piatkowski, T. Fast and accurate polarimetric calibration of infrared imaging polarimetric sensors. *Appl. Opt.* **2021**, *60*, 8499−8512.

(20) Sun, J.; Zhuang, X.; Fan, Y.; Guo, S.; Cheng, Z.; Liu, D.; Yin, Y.; Tian, Y.; Pang, Z.; Wei, Z.; Song, X.; Liao, L.; Chen, F.; Ho, J. C.; Yang, Z. X. Toward Unusual-High Hole Mobility of p-Channel Field-Effect-Transistors. *Small* **2021**, *17*, 2102323.

(21) Wang, W.; Yip, S.; Meng, Y.; Wang, W.; Wang, F.; Bu, X.; Lai, Z.; Kang, X.; Xie, P.; Quan, Q.; Liu, C.; Ho, J. C. Antimony-Rich GaAs$_x$Sb$_{1-x}$ Nanowires Passivated by Organic Sulfides for High-Performance Transistors and Near-Infrared Photodetectors. *Adv. Optical Mater.* **2021**, *9*, 2101289.

(22) Sun, J.; Peng, M.; Zhang, Y.; Zhang, L.; Peng, R.; Miao, C.; Liu, D.; Han, M.; Feng, R.; Ma, Y.; Dai, Y.; He, L.; Shan, C.; Pan, A.; Hu, W. D.; Yang, Z. X. Ultrahigh Hole Mobility of Sn-Catalyzed GaSb Nanowires for High Speed Infrared Photodetectors. *Nano Lett.* **2019**, *19*, 5920−5929.

(23) Ren, Z.; Wang, P.; Zhang, K.; Ran, W.; Yang, J.; Liu, Y.-Y.; Lou, Z.; Shen, G. Z.; Wei, Z. M. Short-Wave Near-Infrared Polarization Sensitive Photodetector Based on GaSb Nanowire. *IEEE Electron Device Lett.* **2021**, *42*, 549−552.

(24) Zhu, X.; Lin, F.; Zhang, Z.; Chen, X.; Huang, H.; Wang, D.; Tang, J.; Fang, X.; Fang, D.; Ho, J. C.; Liao, L.; Wei, Z. Enhancing Performance of a GaAs/AlGaAs/GaAs Nanowire Photodetector Based on the Two-Dimensional Electron-Hole Tube Structure. *Nano Lett.* **2020**, *20*, 2654−2659.

(25) Yang, Z. X.; Han, N.; Fang, M.; Lin, H.; Cheung, H. Y.; Yip, S.; Wang, E. J.; Hung, T.; Wong, C. Y.; Ho, J. C. Surfactant-assisted chemical vapour deposition of high-performance small-diameter GaSb nanowires. *Nat. Commun.* **2014**, *5*, 5249.

(26) Sun, M. H.; Joyce, H. J.; Gao, Q.; Tan, H. H.; Jagadish, C.; Ning, C. Z. Removal of surface states and recovery of band-edge emission in InAs nanowires through surface passivation. *Nano Lett.* **2012**, *12*, 3378−84.

(27) Wu, B.; Xia, G.; Li, Z.; Zhou, J. Sulphur passivation of the InGaAsSb/GaSb photodiodes. *Appl. Phys. Lett.* **2002**, *80*, 1303−1305.

(28) Tsai, C. D.; Lee, C.-T. Passivation mechanism analysis of sulfur-passivated InGaP surfaces using x-ray photoelectron spectroscopy. *J. Appl. Phys.* **2000**, *87*, 4230−4233.

(29) Yang, Z. X.; Yip, S. P.; Li, D. P.; Han, N.; Dong, G. F.; Liang, X. G.; Shu, L.; Hung, T. F.; Mo, X. L.; Ho, J. C. Approaching the Hole Mobility Limit of GaSb Nanowires. *ACS Nano* **2015**, *9*, 9268−9275.

(30) Li, X. D.; Zhang, W. X.; Guo, X. M.; Lu, C. Y.; Wei, J. Y.; Fang, J. F. Constructing heterojunctions by surface sulfidation for efficient inverted perovskite solar cells. *Science* **2022**, *375*, 434−437.

(31) Reiss, P.; Protière, M.; Li, L. Core/Shell Semiconductor Nanocrystals. *Small* **2009**, *5*, 154−168.

(32) Aghdadli, N. K.; Merad, A. E.; Benouaz, T. Adjusted Adashi's Model of Exciton Bohr Parameter and New Proposed Models for Optical Properties of III-V Semiconductors. *American Journal of Materials Science and Technology* **2013**, *3*, 65−73.

(33) Califano, M.; Rodosthenous, P. Theoretical Characterization of GaSb Colloidal Quantum Dots and Their Application to Photocatalytic CO$_2$ Reduction with Water. *ACS Appl. Mater. Interfaces* **2019**, *11*, 640−646.

(34) Miura, N. *Physics of Semiconductors in High Magnetic Fields*; Oxford Science Publications: OUP Oxford, 2008.

(35) Nakamura, Y.; Sugimoto, T.; Ichikawa, M. Formation and optical properties of GaSb quantum dots epitaxially grownon on Si substrates using an ultrathin SiO$_2$ film technique. *J. Appl. Phys.* **2009**, *105*, 014308.

(36) Schmidt, V.; Senz, S.; Gosele, U. Diameter-Dependent Growth Direction of Epitaxial Silicon Nanowires. *Nano Lett.* **2005**, *5*, 931−935.

(37) Rao, C. N. R.; Kulkarni, G. U.; Thomas, P. J.; Edwards, P. P. Size-Dependent Chemistry: Properties of Nanocrystals. *Chem.—Eur. J.* **2002**, *8*, 28−35.

(38) Volokitin, Y.; Sinzig, J.; de Jongh, L. J.; Schmidt, G.; Vargaftik, M. N.; Moiseev, I. I. Quantum-size effects in the thermodynamic properties of metallic nanoparticles. *Nature* **1996**, *384*, 621−623.

(39) Li, Z.; Xia, G.; Wu, B.; Huang, W.; Cheng, Z. Sulfur-passivation mechanism analysis of GaInAsSb photodetectors. *J. Appl. Phys.* **2003**, *94*, 1295−1297.

(40) Gong, X.; Tong, M. H.; Xia, Y. J.; Cai, W. Z.; Moon, J. S.; Cao, Y.; Yu, G.; Shieh, C. L.; Nilsson, B.; Heeger, A. J. High-Detectivity Polymer Photodetectors with Spectral Response from 300nmto1450nm. *Science* **2009**, *325*, 1665−1667.

(41) Lv, L.; Dang, W.; Wu, X.; Chen, H.; Wang, T.; Qin, L.; Wei, Z.; Zhang, K.; Shen, G. Z.; Huang, H. Flexible Short-Wave Infrared Image Sensors Enabled by High-Performance Polymeric Photodetectors. *Macromolecules* **2020**, *53*, 10636−10643.

(42) Zhang, K.; Luo, T.; Chen, H.; Lou, Z.; Shen, G. Z. Au-nanoparticles-decorated Sb$_2$S$_3$ nanowire-based flexible ultraviolet/visible photodetectors. *J. Mater. Chem. C* **2017**, *5*, 3330−3335.

(43) Li, D.; Lan, C.; Manikandan, A.; Yip, S. P.; Zhou, Z.; Liang, X.; Shu, L.; Chueh, Y. L.; Han, N.; Ho, J. C. , Ultra-fast photodetectors based on high-mobility indium gallium antimonide nanowires. *Nat. Commun.* **2019**, *10*, 1664.

(44) Zhang, X.; Huang, H.; Yao, X.; Li, Z.; Zhou, C.; Zhang, X.; Chen, P.; Fu, L.; Zhou, X.; Wang, J.; Hu, W. D.; Lu, W.; Zou, J.; Tan, H. H.; Jagadish, C. , Ultrasensitive Mid-wavelength InfraredPhotodetection Based on a Single InAsNanowire. *ACS Nano* **2019**, *13*, 3492−3499.

(45) Yang, Y.; Peng, X.; Kim, H.-S.; Kim, T.; Jeon, S.; Kang, H. K.; Choi, W.; Song, J.; Doh, Y.-J.; Yu, D. Hot Carrier Trapping InducedNegative Photoconductance in InAs Nanowires toward NovelNonvolatile Memory. *Nano Lett.* **2015**, *15*, 5875−5882.

(46) Guan, X.; Yu, X.; Periyanagounder, D.; Benzigar, M. R.; Huang, J. K.; Lin, C. H.; Kim, J.; Singh, S.; Hu, L.; Liu, G.; Li, D.; He, J. H.; Yan, F.; Wang, Q. J.; Wu, T. , Recent Progress in Short- to Long-Wave InfraredPhotodetection Using 2D Materials and Heterostructures. *Adv. Optical Mater.* **2021**, *9*, 2001708.

(47) Li, L.; Lou, Z.; Shen, G. Z Hierarchical CdS Nanowires Based Rigid and Flexible Photodetectors with Ultrahigh Sensitivity. *ACS Appl. Mater. Interfaces* **2015**, *7*, 23507−23514.

(48) Lou, Z.; Li, L.; Shen, G. Z. Ultraviolet/visible photodetectors with ultrafast, high photosensitivity based on 1D ZnS/CdS heterostructures. *Nanoscale* **2016**, *8*, 5219−25.

(49) Nie, K. Y.; Tu, X.; Li, J.; Chen, X.; Ren, F. F.; Zhang, G. G.; Kang, L.; Gu, S.; Zhang, R.; Wu, P.; Zheng, Y.; Tan, H. H.; Jagadish, C.; Ye, J. Tailored Emission Properties of ZnTe/ZnTe:O/ZnO Core-Shell Nanowires Coupled with an Al Plasmonic Bowtie Antenna Array. *ACS Nano* **2018**, *12*, 7327−7334.

(50) Wang, X. T.; Huang, L.; Peng, Y.; Huo, N.; Wu, K.; Xia, C.; Wei, Z. M.; Tongay, S.; Li, J. B. Enhanced rectification, transport property and photocurrent generation of multilayer ReSe$_2$/MoS$_2$ p−n heterojunctions. *Nano Research* **2016**, *9*, 507−516.

(51) He, T.; Wang, Z.; Cao, R.; Li, Q.; Peng, M.; Xie, R.; Huang, Y.; Wang, Y.; Ye, J.; Wu, P.; Zhong, F.; Xu, T.; Wang, H.; Cui, Z.; Zhang, Q.; Gu, L.; Deng, H. X.; Zhu, H.; Shan, C.; Wei, Z. M.; Hu, W. D. Extrinsic Photoconduction Induced Short-Wavelength Infrared Photodetectors Based on Ge-Based Chalcogenides. *Small* **2021**, *17*, No. e2006765.

(52) Cho, S.; Kang, S.; Pandya, A.; Shanker, R.; Khan, R.; Lee, Y.; Park, J.; Stephen, L.; Craig, S. L.; Ko, H. Large-Area Cross-Aligned Silver Nanowire Electrodes for Flexible, Transparent, and Force-Sensitive Mechanochromic TouchScreens. *ACS Nano* **2017**, *11*, 4346−4357.

(53) Raisch, M.; Genovese, D.; Zaccheroni, N.; Schmidt, S. B.; Focarete, M. L.; Sommer, M.; Gualandi, C. Highly Sensitive, Anisotropic, and Reversible Stress/Strain-Sensors from Mechanochromic Nanofiber Composites. *Adv. Mater.* **2018**, *30*, 1802813.

(54) Zhou, N.; Bekenstein, Y.; Eisler, C. N.; Zhang, D.; Schwartzberg, A. M.; Yang, P. D.; Alivisatos, A. P.; Lewis, J. A. Perovskite nanowire-block copolymer compositeswith digitally programmable polarization anisotropy. *Sci. Adv.* **2019**, *5*, No. eaav8141.

(55) Yao, J.; Yan, H.; Lieber, C. M. A nanoscale combing technique for the large-scaleassembly of highly aligned nanowires. *Nat. Nanotechnol.* **2013**, *8*, 329.

(56) Liu, L. J.; Han, J.; Xu, L.; Zhou, J. S.; Zhao, C. Y.; Ding, S. J.; Shi, H. W.; Xiao, M. M.; Ding, L.; Ma, Z.; Jin, C. H.; Zhang, Z. Y.; Peng, L. M. Aligned, high-density semiconducting carbon nanotube arrays for high-performance electronics. *Science* **2020**, *368*, 850−856.

(57) Fan, Z.; Ho, J. C.; Takahashi, T.; Yerushalmi, R.; Takei, K.; Ford, A. C.; Chueh, Y.-L.; Javey, A. Toward the Development of Printable Nanowire Electronics and Sensors. *Adv. Mater.* **2009**, *21*, 3730−3743.

(58) Fan, Z.; Ho, J. C.; Jacobson, Z. A.; Yerushalmi, R.; Alley, R. L.; Razavi, H.; A, J. Wafer-Scale Assembly of Highly Ordered Semiconductor Nanowire Arrays by Contact Printing. *Nano Lett.* **2008**, *8*, 20−25.

(59) Llerena Zambrano, B.; Forro, C.; Poloni, E.; Hennig, R.; Sivananthaguru, P.; Renz, A. F.; Studart, A. R.; Voros, J. Magnetic Manipulation of Nanowires for Engineered Stretchable Electronics. *ACS Nano* **2022**, *16*, 837−846.

(60) Chen, G.; Liu, Z.; Liang, B.; Yu, G.; Xie, Z.; Huang, H.; Liu, B.; Wang, X.; Chen, D.; Zhu, M. Q.; Shen, G. Z. Single-Crystalline p-Type Zn$_3$As$_2$Nanowires for Field-Effect Transistors and Visible-Light Photodetectors on Rigid and Flexible Substrates. *Adv. Funct. Mater.* **2013**, *23*, 2681−2690.

(61) Zhang, K.; Ding, J.; Lou, Z.; Chai, R.; Zhong, M.; Shen, G. Z. Heterostructured ZnS/InP nanowires for rigid/flexible ultraviolet photodetectors with enhanced performance. *Nanoscale* **2017**, *9*, 15416−15422.

(62) Li, L.; Lou, Z.; Shen, G. Z. Flexible Broadband Image Sensors with SnS Quantum Dots/Zn$_2$SnO$_4$ Nanowires Hybrid Nanostructures. *Adv. Funct. Mater.* **2018**, *28*, 1705389.

(63) Ran, W.; Wang, L.; Zhao, S.; Wang, D.; Yin, R.; Lou, Z.; Shen, G. Z. An Integrated Flexible All-Nanowire Infrared Sensing System with Record Photosensitivity. *Adv. Mater.* **2020**, *32*, 1908419.

(64) Ping, Y.; Long, H.; Liu, H.; Chen, C.; Zhang, N.; Jing, H.; Lu, J.; Zhao, Y.; Yang, Z.; Li, W.; Ma, F.; Fang, X.; Wei, Z. M.; Xu, H. Polarization Sensitive Solar-Blind Ultraviolet Photodetectors Based on Ultrawide Bandgap KNb$_3$O$_8$ Nanobelt with Fringe-Like Atomic Lattice. *Adv. Funct. Mater.* **2022**, 2111673.

(65) Xiao, M.; Yang, H.; Shen, W.; Hu, C.; Zhao, K.; Gao, Q.; Pan, L.; Liu, L.; Wang, C.; Shen, G. Z.; Deng, H. X.; Wen, H.; Wei, Z. M. Symmetry-Reduction Enhanced Polarization-Sensitive Photodetection in Core-Shell SbI$_3$/Sb$_2$O$_3$ van der Waals Heterostructure. *Small* **2020**, *16*, No. e1907172.

(66) Wang, X. T.; Wu, K. D.; Blei, M.; Wang, Y.; Pan, L. F.; Zhao, K.; Shan, C. X.; Lei, M.; Cui, Y.; Chen, B.; Wright, D.; Hu, W. D.; Tongay, S.; Wei, Z. M. Highly Polarized Photoelectrical Response in vdW ZrS$_3$ Nanoribbons. *Adv. Electron. Mater.* **2019**, *5*, 1900419.

(67) Yang, H.; Pan, L. F.; Wang, X. T.; Deng, H. X.; Zhong, M. Z.; Zhou, Z. Q.; Lou, Z.; Shen, G. Z.; Wei, Z. M. Mixed-Valence-Driven Quasi-1D Sn^{II}Sn^{IV}S$_3$ with Highly Polarization-Sensitive UV-vis-NIR Photoresponse. *Adv. Funct. Mater.* **2019**, *29*, 1904416.

(68) Ma, Z.; Chai, S.; Feng, Q.; Li, L.; Li, X.; Huang, L.; Liu, D.; Sun, J.; Jiang, R.; Zhai, T.; Xu, H. Chemical Vapor Deposition Growth of High Crystallinity Sb$_2$Se$_3$ Nanowire with Strong Anisotropy for Near-Infrared Photodetectors. *Small* **2019**, *15*, No. e1805307.

(69) Yang, S.; Wu, M.; Shen, W.; Huang, L.; Tongay, S.; Wu, K.; Wei, B.; Qin, Y.; Wang, Z.; Jiang, C.; Hu, C. Highly Sensitive Polarization Photodetection Using a Pseudo-One-Dimensional Nb$_{(1-x)}$Ti$_x$S$_3$ Alloy. *ACS Appl. Mater. Interfaces* **2019**, *11*, 3342−3350.

(70) Chen, X.; Shehzad, K.; Gao, L.; Long, M.; Guo, H.; Qin, S.; Wang, X.; Wang, F.; Shi, Y.; Hu, W.; Xu, Y.; Wang, X. Graphene Hybrid Structures for Integrated and Flexible Optoelectronics. *Adv. Mater.* **2019**, *32*, 1902039.

(71) Gu, L.; Poddar, S.; Lin, Y.; Long, Z.; Zhang, D.; Zhang, Q.; Shu, L.; Qiu, X.; Kam, M.; Javey, A.; Fan, Z. A biomimetic eye with a hemispherical perovskite nanowire array retina. *Nature* **2020**, *581*, 278−282.

⊞ Recommended by ACS